Heit, B., Koulakov, I., Asch, G., Yuan, X., Kind, R., Alcocer-Rodriguez, I., Tawackoli, S., Wilke, H. (2008): More constraints to determine the seismic structure beneath the Central Andes at 21°S using teleseismic tomography analysis. - Journal of South American Earth Sciences, 25, 1, 22-36,

DOI: 10.1016/j.jsames.2007.08.009.

More constraints to determine the seismic structure beneath the Central Andes at 21°S using teleseismic tomography analysis

B. Heit[1,*], I. Koulakov [1,4], G. Asch,[1], X. Yuan[1], R. Kind[1], I. Alcocer-Rodriguez[2], S. Tawackoli [2], H. Wilke[3].

[1] GeoForschungsZentrum Potsdam, Telegrafenberg, 14473 Potsdam, Germany
[2] Servicio Geológico Minero de Bolivia, Zuazo 1673, 2729 La Paz, Bolivia
[3] Universidad Católica del Norte Departamento de Geologia, Antofagasta, Chile.
[1, 4] Institute of Geology, SB RAS, Novosibirsk, Russia

* Corresponding Author: GFZ, E-226, FAX:+49-3312881277; Telegrafenberg, 14473-Potsdam, Germany. Email: heit@gfz-potsdam.de

E-mail addresses: ivan@gfz-potsdam.de (I. Koulakov), asch@gfz-potsdam.de (G. Asch), yuan@gfz-potsdam.de (X. Yuan), kind@gfz-potsdam.de (R. Kind), ivaralcocer@hotmail.com (I. Alcozer), sohrab@acelerate.com (S. Tawackoli), hwilke@ucn.cl (H. Wilke)

ABSTRACT

A set of seismological stations was deployed in the Central Andes region along a ~600 km long profile at 21°S between Chile and Bolivia and operated for a period of almost two years, from March 2002 to January 2004. Here we present the results of the tomographic inversion for *P*-wave velocity anomalies, based on teleseismic data recorded at the stations. The reliability of the results has been checked by a series of synthetic tests. The tomographic images show high-velocities on the west of the profile that are indicative of cold material from the fore-arc. A low-velocity anomaly is detected at the border between the fore- and the volcanic arc where the Quebrada Blanca seismic anomaly was previously described. This anomaly might be related to the presence of fluids that originate at the cluster of earthquakes at a depth of ~100 km in the subducted plate. A strong low-velocity anomaly is detected beneath the entire Altiplano plateau and part of the Eastern Cordillera, in agreement with previous receiver function results. The Brazilian Shield is thought to be responsible for the strong high-velocity anomaly underneath the Interandean and Subandean regions.

Keywords: Central Andes, Altiplano, *P*- waves, Teleseismic tomography, Velocity anomalies, Lithospheric structure.

1. Introduction

1.1 The Central Andes at 21°S and the Altiplano plateau

The "Cordillera de los Andes" is a long mountain belt that extends for more than 6000 km along the entire western margin of the South American continent. The central part of this orogen between ~3°S and ~47°S is called the Central Andes (e.g. Gansser, 1973; Ramos, 1999) and represents one of the world's best examples of an area that has been formed under the effects of uplift and magmatism arising from the subduction of an oceanic plate (Nazca Plate) under a continental plate (South American Plate) (e.g. Barazangi and Isacks, 1976; Coira et al., 1982; Reutter et al., 1988; Isacks, 1988; Baby et al., 1992, Gubbels et al., 1993; Wigger et al., 1994; Allmendinger et al., 1997). The orogen reaches its greatest width between ~14°S and ~24°S where subduction of the Nazca plate occurs at angles near 20-30° at a rate of 65mm/yr (Cahill and Isacks, 1992; Angermann et al., 1999;). The Central Andes are flanked by flat slab areas to the north (between ~5°S - ~14°S) and to the south (~28°S - ~32°S) where subduction is horizontal to sub-horizontal (e.g. Isacks, 1988; Ramos, 1999). The Altiplano-Puna plateau is the main tectonic feature of the central Andean region and stretches for about ~1700 km from north to south, with an average elevation of ~4 km. The ~400 km wide Altiplano plateau (Figures 1A). is limited to the west by an active volcanic arc (Western Cordillera) and to the east by an active westward verging thick-skinned foreland thrust belt (Eastern Cordillera) (e.g. Allmendinger and Gubbels, 1996; Whitman et al., 1996; Scheuber and Giese, 1999). Further east, the topography descends by steps at the Interandean Zone, the currently active Subandean Fold-Thrust Belt and the Chaco Plain that overlaps progressively with the Precambrian Brazilian Shield (also called Guaporé Shield)

The variable thickness of the crust, the associated shortening, as well as different subduction angles of the subducting plate under the same tectonic conditions have created an elevated plateau with

geological, morphological and magmatic characteristics that enable a differentiation between northern Altiplano (Bolivia and Peru) and Puna in the south (north-western Argentina) (e.g. Allmendinger et al., 1997). The crustal thickness has been investigated by several authors (e.g. Schmitz et al., 1993; Wigger et al., 1994; Zandt et al., 1996; Beck et al., 1996) and reaches ~70-75 km under the Altiplano. Crustal shortening occurring mainly in the Eastern Cordillera (EC) and Subandean region is likely to be responsible for the thickened crust (e.g. Pilger, 1981; Pilger 1983; Isacks, 1988; Reutter et al., 1988; Allmendinger et al., 1997; Sempere et al., 1997; Kley and Monaldi, 1998). Towards the south of the Altiplano a detailed map of crustal thicknesses for the Central Andes based on receiver functions (Yuan et al., 2002) shows that the crustal thickness underneath the southern part of the Puna plateau, is on average 10-15 km shallower than that of the Altiplano. Other projects carried out in the region also provided important results concerning lithospheric structure, crustal-thickness variations and lateral variations in the upper mantle (e.g. Beck et al., 1996; Dorbath et al., 1996; Dorbath and Granet, 1996; Myers et al., 1998; Dorbath and Masson, 2000; Beck and Zandt, 2002). Beneath the plateau, Myers et al., (1998) found low velocities on the eastern side towards the Eastern Cordillera suggesting lithospheric delamination. By combining all geophysical and geological available data McQuarrie et al. (2005) suggested that both the crust and the upper mantle should have played a key role in the lithospheric evolution of the Andean plateau and supported the idea of an ongoing removal of mantle lithosphere beneath the border between the Eastern Cordillera and the Altiplano (Beck and Zandt, 2002).

A series of projects have integrated geological and geophysical methods for investigating subduction related features in the Central Andes (e.g. Isacks, 1988; Jordan et al., 1983; Allmendinger et al., 1997). Steep Angle and wide angle reflection surveys (ANCORP Working Group, 1999; Lüth, 2000; ANCORP Working Group, 2003) and passive seismological networks PISCO 94 (Gräber and Asch, 1999), CINCA 95 (Husen et al., 1999; Patzig, 2000), ANCORP 96 (Haberland and Rietbrock, 2001; ANCORP Working Group, 2003), PUNA97 (Schurr et al., 1999; Schurr, 2000; Schurr et al., 2003; Schurr and Rietbrock, 2004; Schurr et al., 2006), were operated to obtain receiver function (e.g. Yuan et al., 2000)

and local tomographic images (e.g. Koulakov et al., 2006a). The results obtained express clear associations between the passive and active seismic experiments and geological observations. Related to the subduction zone, teleseismic receiver function analysis imaged the oceanic Moho down to a depth of 120 km (Yuan et al., 2000) coinciding with a reduction in seismic activity in the slab at this depth. Short period conversions from local earthquakes extend to depths of 160 km (Bock et al., 2000). Guided waves studies (Martin et al., 2003) also trace a thin wave guide channel above the subducted slab down to a depth of at least 160 km. The ANCORP steep angle reflection profile at 21°S detected the presence of a reflector at a depth of 20 km (~68.5°W) that is thought to be responsible for the Quebrada Blanca Bright Spot (QBBS in ANCORP Working Group, 2003) anomaly but is not observed in gravity data (e.g. Götze et al., 1994; Götze and Kirchner, 1997). Though magneto-telluric soundings do not detect the QBBS anomaly, they show an important conductivity anomaly (Altiplano Conductivity Anomaly) below the Altiplano (Brasse et al., 2002; Haberland et al., 2003). A reflector above the oceanic slab, at a depth of 80 km, has been interpreted as the serpentinization front that delivers rising fluids (ANCORP Working Group, 1999 and 2003; Schilling et al., 2000). Beneath the Altiplano-Puna region, a low-velocity layer has been detected and explained as the possible presence of partial melting material (e.g. Chmielowski et al., 1999; Yuan et al., 2000; Brasse et al., 2002; Zandt et al., 2003). Fluids have also been detected under the active volcanic front and below the Altiplano-Puna plateau and are thought to follow different pathways in the lithosphere (Schurr et al., 2003). On the eastern border of the Altiplano, Wigger et al. (1994) identified west-dipping structures in the crust, also confirmed by Yuan et al. (2000) that are possibly related to the underthrusting of the Brazilian Shield beneath the Subandean and the Eastern Cordillera provinces. This situation has also been suggested by other authors (e.g. Watts et al., 1995; Allmendiger et al., 1997; Lamb et al., 1997). The identification of fault systems or thrusts that penetrate the entire crust as detected by deep-seismic reflection data at 27°S (Cristallini et al., 2004) is still needed to image the distribution of crustal shortening on the eastern part of the Andes at the latitude of the Altiplano. Most of the studies in this area have a lack of geophysical data that may have helped us to image this area over crustal scales. Only geological and structural models based on kinematic studies

suggest that the main thrusts could penetrate as far as the western part of the Eastern Cordillera (e.g. Kley and Monaldi, 1998 and 2002)

In this study, we concentrated on teleseismic inversion for P-velocity anomalies to put more constraints using independent data to confirm and complement results from other projects in the region and to elucidate some features of the Central Andes associated with interacting geological and geodynamical processes.

1.2 **Re**ceiver **Fu**nction **C**entral **A**ndes **Project (ReFuCA): Deployment and Data processing**

During the last funding period of the collaborative research program "Deformation Processes in the Andes" (SFB-267), in cooperation with GFZ Potsdam and in collaboration with South American partners, we deployed and operated a set of 59 seismological stations (March 2002 and January 2004) along a profile at 21°S between the Coast of Chile at ~70°W and the western margin of the Interandean Zone system in Bolivia at ~64.5°W (Figure 1A). The instruments used for this experiment consisted of 47 short-period (SP) RefTek and EDL (Earth Data Logger) equipped with Mark L4-3D seismometers, nine SAM (Storage and Acquisition Module) with broadband (BB) Guralp CMG-3ESP seismometers, and three RefTek equipments operated with CMG-40T type seismometers. The sampling rate was 100 Hz for the SP stations and 50Hz for the BB stations. The spacing of the stations was about 10 km (Figure 1A). A total amount of ~500 GB acquired and converted data were stored in the GEOFON Data Center at GFZ. For teleseismic tomography we used seismic waves generated at epicentral distances between 30° and 95° (Figure 2). Digital waveforms from 154 teleseismic events, located predominantly along the western coast of Central and North America and the Atlantic ridge with $Mw>5$ were obtained from the PDE earthquake catalogue (Preliminary Determinations of Epicenters). The ray coverage was generally well distributed, but towards Antarctica the events were clearly less represented (Figure 2).

Restitution was made for broadband and short-period seismograms to remove the instruments response. After restitution, all *P*- traces were filtered using a pass band of 1-3s (Figure 3).

2. The algorithm of tomographic inversion

Teleseismic tomography is a method that provides information about deep seismic velocity anomalies beneath a selected region, based on the relative delays of seismic arrival times from remote events to the stations located in the study area. This approach was developed in the seventies (e.g. Aki et al., 1977; Aki, 1993) and has since been successfully applied to many different regions in the world (eg. Achauer, 1992; Evans and Achauer, 1993; Koulakov et al., 1995; Wittlinger et al., 1998, Lipptisch et al., 2003; Sandoval et al., 2004). Here, we based our research on a one-step linearized approach, based on the same principle as the ACH algorithm (Aki et al., 1977). However, some peculiarities of the observation system, the configuration and high contrast of the expected velocity anomalies under the Andes required some modifications to the algorithm as we will show.

2.1. Preparation of the residuals

As a preliminary step, the travel-times at teleseismic distances between 30˚ and 95°, with possibly equal steps of epicentral distances are computed according to the 1D Earth model AK-135 (Kennett et al., 1995) and tabulated, from which reference travel-times of the real rays were computed.

The residual time dt corresponding to an i-th source recorded at the j-th station is computed as

$$dt_{ij} = dt_{ij}^{0} - \left[\sum_{j=1}^{N_i} dt_{ij}^{0} \Big/ N_i \right], \qquad [1]$$

where N_i is total number of readings from *i-th* events at the stations of the network. Initial approximation for the residuals is computed as

$$dt_{ij}^{0} = t_{ij}^{obs} - t_{ij}^{ref} - dt_{ij}^{topo} - dt_{ij}^{moho} \qquad .[2]$$

The corrections for the elevation of the stations above sea level, dt^{topo}, are computed as:

$$dt^{topo} = dt^{topo}\sqrt{\sigma^2 - p^2}\,, \qquad [3]$$

where σ is slowness *(1/v)* in the upper-most layer, $p=\sigma \sin \alpha$ is the ray parameter (α is dipping angle) and *dh* is the altitude of the station above sea level.

The corrections for the variable Moho depth along the profile, dt^{moho}, are computed using realistic ray geometry by applying:

$$dt^{moho} = dh^{moho}\left[\sqrt{\sigma_1^2 - p^2} \;\; -\sqrt{\sigma_2^2 - p^2}\right], \qquad [4]$$

where σ_1, σ_2 are the values of slowness below and above the Moho interface, *dh* is a relative Moho depth at the entry point with respect to the average crustal thickness in the reference model. In our case, the Moho depth along 21˚ is from receiver function data (Yuan et al., 2000 and 2002; Heit, 2005; Heit et al., 2007 and Woelbern et al., 2007).

If the absolute value of *dt* in [1] is greater than a predefined value (in our case, 2s) it is considered as an outlier and rejected from further analysis. After this step, the other residuals corresponding to the same event are computed again using [1].

We do not consider the correction for ellipticity of the Earth because the size of the study area is quite small and the ellipticity correction at all stations for one source is practically the same. It could in any case, be included in the source correction term which is obtained during the inversion step.

Average computed values of *P*- residuals for each station after this step and the ray paths of all recorded rays traced down to a depth of 300 km are shown in Figure 1A.

2.2. Algorithm of inversion

In this study, we use the general principle of teleseismic tomography as defined in Aki et al. (1977) and widely known as the ACH algorithm. The inversion is performed based on the rays constructed analytically in a 1D velocity model. The program code used in this study is generally the same as described in Koulakov et al. (2006b), which was applied for investigation of the Dead Sea region.

During the last years, non-linear algorithms based on *iterative* inversion with 3D ray tracing have been actively developed (e.g. Lipptisch et al., 2003, Sandoval et al., 2004). We consider that in our case, however, the linear approach is sufficiently precise. Indeed, when the iterative non-linear approach is performed, the ray path is only perturbed in the upper mantle. We also perform a synthetic test which shows that the difference between the ray paths in 1D and 3D models in the upper mantle with a velocity anomaly ~5% amplitude is not more than 10 km. The travelling through anomalies of 50-100 km size, which can be resolved by our observation system, 3D and 1D rays would provide practically the same residuals. In some studies, as those by Lipptisch et al. (2003) and Sandoval et al. (2004), the data allow much higher resolution. In these cases perturbations of the ray paths can be of the same order as the resolved anomalies, thus utilization of 3D ray tracing is well grounded.

The upper and lower limits of the resolved area in teleseismic studies are determined fairly unambiguously. The upper limit is a depth where the rays from neighboring stations (at some average spacing) start to intersect with each other. In Figure 1A and 1B we show the distribution of the piercing points of the rays at 20 km depth. To estimate the “mixing” of rays from different stations at this depth, the points corresponding to odd and even stations are indicated with different colors (red and blue, respectively). It could be seen that our station spacing provide satisfactory intersections to use the 20 km depth level as the upper limit of the study volume. The resolution limit of the teleseismic experiment reaches its deepest point where the rays from the most remote stations of the network can intersect with

each other. Roughly, the upper limit is set as the average spacing between stations and the maximum depth equals to ~ 0.7 × size of the network. According to these estimations, the depth range of the resolved area in our case is between 20 km and ~200 km.

The resulting velocity model was computed in nodes of a parameterization grid distributed in some depth levels according to the ray density, as described in Koulakov (1998) and Koulakov et al. (2002). Between these levels, the anomalies are linearly interpolated and the first layer is set at 20 km depth. We assume that the velocities at 20 km depth reflect crustal effects between 0 and 20 km. For example, an anomaly between 0-5 km depth would cause the same effect in the result as an anomaly between 15-20 km depth. In our model, a zero anomaly is set at 0 km depth. However, it should be noted that the vertical change in velocity anomaly in the uppermost layer (0-20 km) has no direct interpretation.

Although the lower limit of the resolved area is estimated at ~200 km depth, we install the parameterization nodes down to 300 km depth. We suppose that the velocity values in nodes below 200 km depth take most of the outside effects, which can be also included in the source corrections. In the grid search, we used constant 15 km steps between the depth levels. In each depth level, the nodes were fixed according to the ray density. However, to avoid an excessive concentration of nodes in the area of ray fluctuations, we fixed the minimal 15 km distance between the nodes. Examples of the grid construction according to the ray density for three depth levels are shown in Figure 4. Velocity distribution between nodes was defined using bilinear interpolation. The number of nodes at each depth level depends upon the value of the fixed minimal spacing and varied from about 70 at shallowest level to 100 at deeper levels.

The matrix elements responsible for the velocity variations, M^V, are computed on the basis of the ray paths traced in the 1D spherical-velocity model as:

$$M_{ij}^{Vp(s)} = -\frac{1}{\Delta V_j^{p(s)}} \int_{\gamma_i} \frac{\Delta U_j(s)}{V_0^2(s)} ds \quad , \qquad [5]$$

where *i* is the ray number (row of the matrix), *j* is the node number (column of the matrix), γ_i is the ray path, S is a point on the ray, $\Delta V_j^{p(s)}$ is the unit velocity variation at the *j*-th node, $\Delta U_j(s)$ is the velocity variation at the current point of the ray due to velocity variations at the j-th node and $V_0(s)$ is the reference velocity at the current point.

An additional block of the matrix allows the regularization of the smoothness of the obtained 3D velocity distribution. Each line in this block contains two non-zero elements with opposite signs, corresponding to neighboring nodes in the model and zero data vector. Increasing the weight of these elements has a smoothing effect upon the resulting anomalies. Determination of all the coefficients for the inversion is crucial. The total formalization of their definition seems to be not possible. In our case, we define the coefficients using the results of synthetic tests with realistic values of parameters and noise level.

3. Synthetic tests

The synthetic testing is a very important step in data analysis that is performed simultaneously to the observational data inversion. By executing a synthetic test, it is possible to explore vertical and horizontal resolutions that provide essential information about the trustworthiness of the features in the final inversion of the real data. In addition, synthetic tests also provide optimal estimations of the parameters used for the real data inversion.

3.1. Methodology used for synthetic testing

Here we present results for two types of tests corresponding to horizontal and vertical anomalies that aim to reconstruct the presence of realistic anomalies expected in the study area (e.g. crustal, lithospheric features and the oceanic slab). The synthetic tests are performed using the same geometry (earthquake/stations) as in the case of the observed data set. The residual times for these tests are computed along the actual rays as:

$$dt = \int_{\gamma} \Delta\sigma(\gamma) dS + \tau^{stat} + \tau^{srce} + \varepsilon \qquad [6]$$

where $\Delta\sigma(\gamma)$ is a perturbation of the slowness in the initial synthetic model at a point of the ray, τ^{stat} and τ^{srce} are the station and source terms, respectively, and ε is the random noise. Station and source terms are defined as:

$$\tau_i = ab_i \qquad [7]$$

where a is a constant providing a predefined standard deviation of the corrections and b_i are random numbers. In our case, we used a periodic repetition of the following seven numbers: 3, -1, 2, -2, 1, -3, 0 which are normalized with a coefficient k that provides a predefined value of standard deviation for station corrections. The random noise ε is produced by a random number generator which provides a statistical distribution similar to that of the actual residuals with predefined average amplitude.

3.2. Synthetic tests for horizontal and vertical anomalies

To check the capacity of the algorithm to reconstruct horizontal anomalies we perform the checkerboard test. The initial model is represented by alternating columns with positive and negative velocity

anomalies. Vertically they are unlimited. For checking the *P*- velocity models we used the lateral size of anomalies at 100×100 km. The amplitude of the anomalies was ±3%. We added noise with rms of 0.3s. The results of reconstruction (Figure 5) show rather reliable reconstruction of the anomalies around the profile in all sections down to ~200 km depth. Below this depth the anomalies are strongly smeared and disappear in most parts of the study volume. From this test for P-wave velocities, we observe an acceptable horizontal resolution to reconstruct features of 100 km size in the depth interval from 20 to 200 km.

For estimating vertical resolution, we performed a vertical checkerboard test (Figure 6) where the anomalies are defined as unlimited horizontally oriented anomalous blocks of ±3% amplitude. These alternated blocks of 80x80 km size are separated from each other with 20 km zones of zero values (Figure 6A). The conditions for the inversion were the same as in the test with horizontal checkerboard described above. The result of the synthetic inversion is shown in Figure 6B. It can be seen that the vertical resolution provided by our observation system is rather good and allows correct reconstruction of the main patterns in the study volume.

In the next test (Figure 7) we explore the capacity of algorithm to resolve real shaped patterns. Figure 7A presents the configuration of the initial synthetic model in a vertical section. This model contains different bodies, reproducing the existence of some realistic anomalies (e.g. volcanic arc, Brazilian Shield and Altiplano). Random noise (0.3, 0.2, 0.2 of rms for ε, τ^{stat} and τ^{srce} terms respectively) was added according to the formula shown in [6]. The variance reduction after performing this test was approximately the same as the one obtained during the real data processing (~60 %).

The results of inversion (Figure 7B) show that the position of the bodies can be well reconstructed. However, the crustal bodies are strongly smeared downwards due to insufficient vertical resolution. For example, the positive anomaly in the upper mantle, on the eastern side of the profile, is poorly resolved.

This effect could be partially induced by the smearing of the large low-velocity "Altiplano" block. Furthermore, the "slab" anomaly is poorly reconstructed. To clarify this situation, we investigate the problem of the ill resolved slab in the next section.

3.3. Reconstruction of slab

Here we explore the capacity of the observation system to resolve the slab which appears to be one of the brightest features in the study volume. We define the top of the subducted slab as an envelope of seismicity (hypocenters) located by Engdahl et al. (1998) (Figure 8A). The shape of the slab is also defined by receiver function data from the ReFuCA dataset (Heit, 2005; Heit et al., 2007; Woelbern et al., 2007). The thickness of the oceanic lithosphere was fixed at ~100 km according to a worldwide plot of age versus thickness for oceanic lithosphere from Turcotte and Schubert (1982). The slab was defined down to 700 km depth and the synthetic residuals where computed for rays down to this depth while the inversion area was defined down to 300 km. This means that the investigated area for our profile of stations does not provide any resolution for depths greater than 300 km, but the rays are still affected by the presence of the slab outside the study volume.

The reconstruction of the slab using data without noise shows limited capacity of the teleseismic algorithm to reconstruct such kind of anomalies, which in our case, is strongly shifted upwards (Figure 8B). We are not able to resolve the slab anomaly because we lack of favorable ray configuration. This means that, rays traveling to the west will cross the slab almost perpendicularly and produce similar residuals for these rays at all stations which then become zero after reducing with respect to the average value. For the rays traveling to the east, only stations in western part of the profile can "feel" or reproduce the slab but, in the mantle, they intersect with rays that have zero residuals. Therefore, the inversion shifts upwards the slab related anomaly, as observed in the results of the slab reconstruction (Figure 8B).

At the same time, the variance reduction after inversion proved to be 97%, indicating that, the initial and reconstructed anomalies provide practically the same values of residuals along the rays used in the data set. This fact can be used to test the effect of the slab anomaly on the interpreted data by reducing the influence of some parameters so they can be evaluated from independent information during the real data inversion.

4. Inversion of observed data

The results of inversion using the residuals computed for 1D model is shown in Figure 9A. In this figure we do not see a clear image of the slab. As described previously, the poor resolution of the teleseismic inversion for reconstructing the slab-shaped anomaly (Section 3.3.) suggests we are unable to obtain a clear image of the slab from our data set. However, the a-priori information about the position of the slab can be used to subtract the effect of the slab from the real data inversion. The formalism used to subtract the effect of the slab needs some additional explanations. The possibility of effecting such a subtraction is based on the linearity of the inverse and forward tomographic operators. In linear approach, the inversion is performed on the basis of the rays constructed in the reference model (usually a 1D model).

We denote the direct operator A as a solution of forward problem, $dt = A(dv)$, where dv is the velocity model and dt are the residual times, and the inverse operator A^{-1} as a solution of the inverse problem: $dv = A^{-1}(dt)$. Both direct and inverse operators are assumed to be linear and therefore:

$$dv_1 = A^{-1}\, dt^{obs} \qquad [8]$$

and

$$dv_2 = A^{-1}(dt^{obs} - dt^{slab}) + A^{-1}(dt^{slab}) \qquad [9]$$

should be equal. Here dt^{obs} means the observed residuals, and dt^{slab} are the residuals computed by integration through the slab. The correspondence between $dv_1 \sim dv_2$ is illustrated in Figures 9A and 9B. If we now apply a direct linear tomographic operator to these two velocity models, we obtain the following residuals:

$$dt_1 = A[dv_1] = A[A^{-1}\, dt^{obs}] \qquad [10]$$

$$dt_2 = A[dv_2] = A[\, A^{-1}(dt^{obs} - dt^{slab})] + A[A^{-1}(dt^{slab})] \qquad [11]$$

which should also be equal; that is $dt_1 = dt_2$.

At the same time, in the synthetic test with reconstruction of the slab, we have shown that the variance reduction of such an inversion is 97%. This means that

$$dt^{slab} \sim A\,(A^{-1}\, dt^{slab}) \qquad [12]$$

with maximum errors of 3%. However, we should note that

$$dv^{slab} \neq A^{-1}\, dt^{slab} \qquad [13]$$

due to poor vertical resolution, and thus the slab is smeared upwards. We introduce a modification to equation [9] using dv^{slab}, and obtain a new velocity model:

$$dv_3 = A^{-1}(dt^{obs} - dt^{slab}) + dv^{slab} \qquad [14]$$

which is shown in Figure 9C and is obviously different from dv_2 results (due to the differences shown in [13]). At the same time, the residuals after application of the direct tomographic operator

$$dt_3 = A[dv_3] = A[\, A^{-1}(dt^{obs} - dt^{slab})] + A[dv^{slab}] \qquad [15]$$

are approximately equal to dt_2 in [11] with an accuracy of 3% (97% of variance reduction). This means that three velocity models, dv_1, dv_2 and dv_3, provide similar residuals and therefore can be equally used to explain the observed residuals dt^{obs}. Results for dv_3 (Figure 9C), however, provide the best results.

Since the approximate shape and amplitude of the velocity contrast for the slab in our studied area are known, we decided to use this information in our starting model.

5. Discussion

In the tomographic images, we presented the results in vertical (Figures 9A-C) and horizontal sections (Figure 10). It should be noted that for the depth down to 80 km we observe fairly good correlation with the results of local tomography inversion (Koulakov et al., 2006a). For the discussion, we will focus our attention on the detected anomalies with respect to their position from west to east (Figure 11A):

1- The west region (Costal Cordillera, Longitudinal Valley and Precordillera) is characterized by the presence of a pronounced high *P*- wave velocity anomaly, to a depth down to 60 km, in good correlation with the Chilean Coastal Cordillera and part of the Longitudinal Valley. This anomaly is located in the fore-arc and could be related to the presence of the Jurassic volcanic arc which developed on Precambrian-Paleozoic crust (e.g. Troeng et al., 1994; Lamb and Hoke, 1997). The interaction between the subducted oceanic plate and the continental crust must be responsible for the high velocities observed in this region.

2- The limit between high-velocity anomalies to the west and low-velocities towards the east, at approximately 69°W, corresponds with the location of the West Fissure (WF) on the surface, close to the eastern border of the Precordillera. The WF is usually described as a sub-vertical strike-slip fault system integrating the Precordilleran Fault System (e.g. Scheuber and Reutter, 1992; Scheuber et al., 1994; Reutter et al., 1996; Victor et al., 2004). The change in relative velocities west and east of the WF indicates variations in the composition of the rocks and thermal state of the materials across these faults. The WF probably represents the border between blocks of different temperature. Schurr and Rietbrock (2004) found similar results for the Atacama Block in the south of our study area.

Between the WF and the Western Cordillera a low-velocity anomaly has been detected that virtually emanates from the subducted plate and coincides with the position of an anomalous reflective body detected by seismics at depths of 15 to 25 km and interpreted as the Quebrada Blanca Bright Spot (QBBS in ANCORP Working Group, 1999). Due to its shape and position, between ~69° and 68°W, we also interpreted this low- velocity anomaly as the QBBS (Figure 11A), which is presumably indicating the presence of fluids or magmatic bodies related to the volcanic front of the Central Volcanic Zone (CVZ). Beneath the border between the CVZ and the western limit of the Altiplano plateau a high velocity body can be recognized (Figure 11A) coinciding with the position of high velocity Neogene volcanic material (Dorbath and Masson, 2000) and the presence of Precambrian basement on the western side of the Altiplano (Troeng et al., 1994).

3- The Altiplano plateau is characterized by a prominent low-velocity anomaly Figure (11A). The shape and position of the Altiplano anomaly seems to be strongly controlled by the presence of the Uyuni-Kenayani Fault Zone (UKFZ) at ~67°W (e.g. Sempere et al., 1990; Elger et al., 2005). The presence of a low-velocity layer or Altiplano Low-Velocity Zone (ALVZ) has already been described beneath the Altiplano and adjacent areas (Wigger et al., 1994; Yuan et al., 2000) and is also present in our data, extending from ~68°W to ~65°W. The extension of this layer towards the east could also be affected by the presence of the Main Andean Thrust (MAT), also called Interandean Thrust (e.g. Mertmann et al., 2001; Scheuber et al., 2006). The MAT is a prominent detachment zone located at the border between the Eastern Cordillera (EC) and the Inter- Subandean units (e.g. Allmendinger et al., 1997). A thermally weakened crust should facilitate a decoupling surface to reach the ALVZ and in this way, sub-horizontal shear zones will be able to transfer shortening eastward along a decoupling surface (e.g. Elger, 2003; Victor et al., 2004; Elger et al., 2005). The detachments have been clearly imaged by seismic refraction (Wigger et al., 1994) and could be responsible for zones where changes in lithostatic pressure, material state of the rocks and temperature variations affect the configuration of fluids that move along these structures in the interior of the crust.

4- The Eastern Cordillera presents what we interpret as an extension of the ALVZ towards the east of the Altiplano (Yuan et al., 2000; Brasse et al., 2002; Haberland et al., 2003). The anomaly is located at the same depth of the ALVZ and extends between ~67°W and ~65.5°W.

At ~66°W and underneath the receiver function Moho (Yuan et al., 2000 and 2002) a low- velocity anomaly (low velocity materials in Figure 11B) could be indicating that magmatic additions are taking place at the base of the continental crust. In combination with other geological and geotectonic processes, these additions should play an important role in crustal growth. Although the Moho topography obtained from receiver function supports this idea (the Moho deepens beneath this area), it has long been estimated that magmatic addition from arc production represents ~1 % of the crustal thickness (Trumbull, pers. comm.).

Between 100 and 150 km depth at ~65°W we detect relatively low velocities on the tomographic images (see Figure 11A and 11B) that we interpret as asthenospheric low velocity materials. Although the position of these low velocities is not well constrained (due to smearing), it is important to note that it coincides with the region where data from receiver function (Heit et al., 2007) shows an abrupt thinning of the lithosphere-astenosphere boundary and where Myers et al. (1998) detected the presence of a zone of high attenuation-low velocities, which they interpreted as materials under near solidus conditions. Beck and Zandt (2002) proposed a removal of the lithosphere at this latitude, later confirmed by McQuarrie et al. (2005), while Hoke et al. (1994) postulated the existence of a thin lithosphere at 20°S for parts of the EC to explain elevated ^{3}He signature in geothermal systems. All these observations seem to indicate the presence of anomalous velocities that might reflect the presence in this region of asthenospheric materials.

The presence of anomalous materials in the upper mantle-lower crust region could be related to the idea of lithospheric removal or delamination, originally introduced to explain the presence of elevated

plateaus, as Tibet or Altiplano-Puna (e.g., Bird, 1979; Kay and Kay, 1993). In the case of delamination, thick and cold lithosphere delaminates or separate from the base of the continental crust and sinks into the asthenosphere, process that is usually associated with uplift and mafic magmatism.

5- In the east of the Eastern Cordillera and at the position of the Main Andean Thrust (MAT), we detect the presence of a strong, high-velocity anomaly, that we interpret as the Brazilian Shield - also called the Guaporé Shield covered by Neogene sediments filling the basins from the Interandean, Subandean and Chaco Plain provinces (Figures 11A and 11B). The presence at this longitude of the Brazilian Shield has also been proposed by other authors (e.g. Wigger et al., 1994; Watts et al., 1995; Lamb et al., 1997; Beck and Zandt, 2002; McQuarrie et al., 2005).

We assume that the Brazilian Shield, as a cold and old unit underlying the before mentioned sediments, is responsible for the observed anomaly. Unfortunately, the resolution of the upper and deeper parts of the anomaly is not sufficient to determine if there is some type of deformation structure present. Therefore, underthrusting of the Brazilian lithosphere can not be recognized in the tomographic images. The border between the Brazilian Shield with high velocities and the Eastern Cordillera with low velocities appears to indicate that shortening occurred mainly in this region. A flexurally strong lithosphere, as suggested by Watts et al. (1995), should play a key role in the configuration of the Brazilian Shield anomaly and explain foreland deformation in the thin-skinned fold-and-thrust belt. The Interandean, the Subandean and Chaco morphological units could therefore be situated above a series of detachments where great amounts of shortening may have taken place.

6. Conclusions

The tomographic images of the profile along 21°S confirm previous observations about the presence of a low-velocity layer in the upper crust below the Altiplano (Altiplano Low-Velocity Zone) and shows that this zone may extend towards the Eastern Cordillera where a similar low-velocity body has been

detected (Figure 11B). A possible relationship between this low-velocity zone and the anomalies observed to the west, at the same depth and beneath the volcanic arc, can also be interpreted from the tomographic results. The origin of this low-velocity layer remains poorly understood.

The position and distribution of the low-velocity anomaly located beneath the volcanic arc that emanates from the Benioff zone at depths of ~100 km could be indicating that fluids are being released by earthquakes that take place due to phase transformations (e.g. eclogite). The fluids originate in adjacent areas of a prominent cluster of earthquakes and probably move towards the volcanic arc in a more vertical way. This ascent path could also be indicating temperature differences in the lithosphere that forces the fluids to move along pre-existing weakened zones in the crust. The position of this feature coincides with the previously described Quebrada Blanca Bright Spot anomaly determined by seismics. We note that this anomaly has been detected by two different experiments, i.e. seismic (e.g. ANCORP Working Group, 1999) and teleseismic (this results), which provides more evidence of its existence (Figure 11B).

The sharp limits between high- and low-velocities in the crust could be related to the presence of major lineaments and deep reaching fault systems (e.g. the Main Andean Thrust, Western Fissure). This situation is observed at both ends of the profile, where the high-velocity block of the fore-arc and the Brazilian Shield are located (Figure 11B).

The tomographic images do not show any evidence supporting the underthrusting of the Brazilian lithosphere as suggested by some authors. The presence of anomalous velocities beneath the lithosphere-asthenosphere boundary at depths of ~150 km correlates well with observations from other authors but we are not able to determine if this is associated with the detachment or delamination of lithospheric material.

Unfortunately, we are not able to get reliable information about the slab because the length of the profile

is too short for this purpose. This problem is well known as the slab or any sub-horizontal structure cannot be reliably recovered (e.g. Evans & Achauer, 1993). In our case, we do not image the position of the slab nor its geometry and we demonstrate that by using the a-priori information about the position of the slab we are able to subtract the effect of the slab from the observed data.

Acknowledgments: We would like to thank the people from the different villages in Bolivia and Chile for permitting us to deploy the stations for those long and pleasant two years on the field and particularly to Max Cayo Vilca in San Juan del Rosario and Felipe our driver from La Paz. This research was supported by the last funding period of the SFB-267 (FU-Berlin and GFZ Potsdam in Germany). We would like to thank the Geophysical Instrument Pool, Potsdam (GIPP) for providing the seismic equipment. The manuscript benefited very much from the comments and remarks from the reviewers P. Alvarado and E. Cristallini and the journal editor V. Ramos.

REFERENCES

Achauer, U., 1992. A study of the Kenya rift using delay time tomography analysis and gravity modelling. Tectonophysics 209, 197-207.

Aki, K., Christofferson, A., Husebye, E.S., 1977. Determination of the three dimensional structure of the lithosphere. J. Geophys. Res., 82 277-296.

Aki, K., Seismic Tomography: Theory and Practice, 1993. Ed. by Iyer, H.M., Hirahara, K., Chapman , Hall, London, pp. 842.

Allmendinger, R. W. and Gubbels, T., 1996. Pure and simple shear plateau uplift, Altiplano-Puna, Argentina and Bolivia. Tectonophysics, 259, 1-13.

Allmendinger, R.W., Jordan, T.E., Kay, S. M, Isacks, B., 1997. The evolution of the Altiplano-Puna Plateau of the Central Andes. Annu. Rev. Earth Planet. Sci. 25, 139-174.

ANCORP Working Group, 1999. Seismic reflection image of the Andean Subduction Zone Revealing Offset of Andean subduction-zone earthquake locations into oceanic mantle, Nature 397, 341-344.

ANCORP Working Group, 2003. Seismic imaging of a convergent continental margin and plateau in the Central Andes (Andean Continental Research Project 1996 (ANCORP ´96), J. Geophys. Res. 108, 2328, doi:10.1029/2002JB001771.

Angermann, D., Klotz, J., Reigber, C., 1999. Space-geodetic estimation of the Nazca-South America Euler vector, Earth Planet. Sci. Lett., 171, 329-334.

Baby, P., G. Hérail, R. Salinas, T. Sempere, 1992. Geometry and kinematic evolution of passive roof duplexes deduced from cross section balancing: Example from the foreland thrust system of the southern Bolivian subandean zone, Tectonics, 11(3), 523–536.

Barazangi, M. and Isacks, B.L., 1976. Spatial distribution of earthquakes and subduction of the Nazca plate beneath South America. Geology 4, pp. 686–692

Beck, S.L., Silver, P.G., Drake, L., Zandt, G, Myers, S.C., Wallace, T.C., 1996. Crustal-thickness variations in the central Andes, Geology 24, 407-410.

Beck, S. and G. Zandt, 2002. The nature of orogenic crust in the central Andes, J. Geophys. Res. 107(B10), 2230.

Bird, P., 1979. Continental delamination and the Colorado Plateau, J. Geophys. Res., 84, 7561-7571.

Bock, G., Schurr, B., Asch, G., 2000. High-resolution receiver function image of the oceanic Moho in the subducting Nazca plate from P-to S- converted waves, Geophys. Res. Lett. 27, 3929-3932.

Brasse, H., Lezaeta, P., Rath, V., Schwalenberg, K., Soyer, W., Haak, V., 2002. The Bolivian Altiplano conductivity anomaly, J. Geophys. Res., 107, doi: 10.1029/ 2001JB000391.

Cahill, T. and Isacks, B., 1992. Seismicity and shape of the subducted Nazca plate, J. Geophys. Res., 97, 17,503-17,529.

Chmielowski, J., Zandt, G., Haberland, C., 1999. The Central Andean Altiplano-Puna magma body, Geophys. Res. Lett., 26, 783-786.

Coira, B., Davidson, J., Mpodozis, C., Ramos, V., 1982. Tectonic and magmatic evolution of the Andes of northern Argentina and Chile, Earth Sci. Rev., 18pp, 303-332.

Cristallini, E. O., A. H. Comínguez, V. A. Ramos, E. D. Mercerat, 2004. Basement double-wedge thrusting in the northern Sierras Pampeanas of Argentina (27°S) - Constraints from deep seismic reflection, in Thrust Tectonics and Hydrocarbon Systems, edited by K. R. McClay, AAPG Mem., 82, 65–90.

Dorbath, C., and M. Granet, 1996. Local earthquake tomography of the Altiplano and Eastern Cordillera of northern Bolivia, Tectonophysics, 259, 117 –136.

Dorbath, C., Paul, A. and the Lithoscope Andean group, 1996. Tomography of the Andean crust and mantle at 20°S: First results of the Lithoscope experiment, Phys. Earth Planet. Inter., 97, (1-4).

Dorbath, C. and Masson, F., 2000. Composition of the crust and upper-mantle in the Central Andes (19.5°S) inferred from P wave velocity and Poisson's ratio, Tectonophysics, 327, 213-223.

Elger, K., 2003. Analysis of deformation and tectonic history of the Southern Altiplano Plateau (Bolivia) and their importance for plateau formation, PhD -Scientific Technical Report, (STR03/05). GeoForschungsZentrum, Potsdam.

Elger, K., Oncken, O., Glodny, J., 2005. Plateau-style accumulation of deformation: Southern Altiplano. Tectonics, 24, TC4020, doi:10.1029/2004TC001675.

Engdahl, E., van der Hilst, R., Buland, R., 1998. Global teleseismic earthquake relocation with improved travel times and procedures for depth determination, Bull. Seism. Soc. Am. 88, 722-743.

Evans, J., Achauer, U., 1993. Teleseismic velocity tomography using the ACH method: theory and application to continental scale studies, In: Iyer, H., Hirahara, K. (Eds.). Seismic tomography: Theory and Practice, Chapman & Hall, London, pp. 319-360.

Gansser, A., 1973. Facts and Theories on the Andes, Journal of the Geological Society, 129, pp. 93 131.

Götze, H.-J, Lahmeyer, B., Schmidt, S., Strunk, S., 1994. The lithospheric structure of the Central Andes (20-26S) as inferred from quantitative interpretation of regional gravity, In: Tectonics of the Southern Central Andes, in: K.-J. Reutter, E. Scheuber, P.J. Wigger (Eds), Springer-Verlag, New York, pp. 7-21.

Götze, H-J. and Kirchner, A., 1997. The Gravity Field at the Continental Margin of South America (20° to 29° S),.Proceedings of the 30th International Geological Congress, in: Ed. Hong Dawei, (4) Utrecht, pp.135-141.

Graeber, F. and Asch, G., 1999. Three-dimensional models of P wave velocity and P-to-S velocity ratio in the southern central Andes by simultaneous inversion of local earthquake data, J. Geophys. Res. 104, 20237-20256.

Gubbels, T., Isacks, B., Farrar, E., 1993. High level surfaces, plateau uplift and foreland development, Bolivian central Andes, Geology, 21, 695-698.

Haberland, C. and Rietbrock A., 2001. Attenuation tomography in the western Central Andes: A detailed insight into the structure of a magmatic arc, J. Geophys. Res., 106, 11151-11167.

Haberland, C., Rietbrock, A., Schurr, B., Brasse, H., 2003. Coincident anomalies of seimic attenuation and electrical resistivity beneath the southern Bolivian Altiplano plateau, Geophys. Res. Lett., 30, doi:10.1029/2003GL017492.

Heit, B., 2005. Teleseismic tomographic images of the Central Andes at 21°S and 25.5°S: an inside look at the Altiplano and Puna plateaus, Ph.D Thesis, Freie Universitaet Berlin, Scientific Technical Report (STR06/05), GeoForschungsZentrum, Potsdam- Germany.

Heit B., Sodoudi, F., Yuan, X., Bianchi, M., Kind, R., 2007. An S receiver function analysis of the lithospheric structure in South America, Geophys. Res. Lett., 34, L14307, doi:10.1029/2007GL030317.

Hoke, L., Hilton, D.R., Lamb, S.H., Hammerschmidt, K., Friedrichsen, H., 1994. 3He evidence for a wide zone of active mantle melting beneath the Central Andes, Earth Planet. Sci. Lett., 128, 341-355.

Husen, S., Kissling, E., Flueh, E., Asch, G., 1999. Accurate hypocenter determination in the seismogenic zone of the subducting Nazca Plate in Northern Chile using a combined on-/offshore Network, Geophys.

J. Int., 138, 687-701.

Isacks, B., 1988. Uplift of the Central Andean plateau and bending of the Bolivian orocline, J. Geophys. Res., 93, 3211-3231.

Jordan, T.E., Isacks, B., Ramos, V.A., Allmendinger, R.W., 1983. Mountain building in the Central Andes, Episodes 3, 20-26.

Kay, R. and Kay, S. M., 1993. Delamination and delamination magmatism, Tectonophysics, 219, 177-189.

Kennett, B. L.,. Engdahl, E. R., Buland, R., 1995. Constraints on seismic velocities in the Earth from travel times, Geophys. J. Int., 122, 403-416.

Kley, J. and Monaldi, C., 1998. Tectonic shortening and crustal thickness in the Central Andes: How good is correlation?, Geology, 26, 723-726.

Kley, J. and Monaldi, C., 2002. Tectonic inversion of the Santa Barbara System of the central Andean foreland thrust belt, northwestern Argentina, Tectonics, 21(6), doi:10.1029/2002TC902003.

Koulakov, I. Yu., Tychkov, S.A., Keselmann, S.I., 1995. Three-dimensional structure of lateral heterogeneities in *P*-velocities in the upper mantle of the southern margin of Siberia and its preliminary geodynamical interpretation, Tectonophysics, 241, 1, 239-257.

Koulakov, I. Yu., 1998. 3D tomographic structure of the upper-mantle beneath the central part of Eurasian continent, Geophys. J. Int., 133, 467-489.

Koulakov, I. Yu., Tychkov, S., Bushenkova, N., Vasilevskiy, A., 2002. Structure and dynamics of the upper mantle beneath the Alpine-Himalayan orogenic belt, from teleseismic tomography, Tectonophysics, 358, 77-96.

Koulakov, I., Sobolev, S., Asch, G., 2006a. *P*- and *S*-velocity images of the lithosphere-asthenosphere system in the Central Andes from local-source tomographic inversion, Geophys. J. Int, 167, 106–126.

Koulakov, I., Sobolev, S.V., Weber, M., Oreshin, S., Wylegalla, K., Hofstetter, R., 2006b. Teleseismic tomography reveals no signature of the Dead Sea Transform in the upper mantle structure, Earth Planet. Sci. Lett., 252, 189-200, 2006.

Lamb, S., Hoke, L., Kennan, L.; Dewey, J., 1997. Cenozoic evolution of the Central Andes in Bolivia and northern Chile, Orogeny through time. Geological Society of London, J. P. Burg, M. Ford (Eds), Special Publication, London, vol. 121, pp. 237-246.

Lamb, S. and Hoke, L., 1997. Origin of the high plateau in the central Andes, Bolivia, South America, Tectonics 16, 623-649. 10.1029/97TC00495.

Lippitsch, R., Kissling, E., Ansorge, J., 2003. Upper-mantle structure beneath the Alpine orogen from high-resolution teleseismic tomography, J. geophys. Res., 108(B8), 2376–2390.

Lüth, S., 2000. Ergebnisse weitwinckelseismischer Untersuchungen und die Struktur der Kruste auf einer Traverse über die Zentralen Anden bei 21 Grad S, Berliner Geowissentschaftliche Abhandlungen, 37, Reihe B.

Martin, S., Rietbrock, A., Haberland, C., Asch, G., 2003. Guided waves propagating in subducted oceanic crust, J. Geophys. Res., 108, doi:10.1029/2003JB002450.

McQuarrie, N., Horton, B., Zandt, G., Beck, S., DeCelles,P., 2005. Lithospheric evolution of the Andean fold-thrust belt, Bolivia and the origin of the central Andean plateau, Tectonophysics 399, pp. 15–37.

Mertmann, D., Scheuber, E. Ege, H., Silva, P., Reutter K-J., Sobel, E., Jacobshagen, V., 2001. Tectono-sedimentary evolution of the southern Altiplano: basin evolution, thermo-chronology and structural geology, Interaction between endogenic and exogenic processes during subduction orogenesis. SFB-267.Deformation Processes in the Andes, Report Volume 1999-2001 (2001) 25-50.

Myers, S., Beck, S., Zandt, G. and Wallace, T., 1998. Lithospheric-scale structure across the Central Andes of Bolivia from seismic velocity and attenuation tomography, J. Geophys. Res. 103, 21,233-21,252.

Patzig,. R., 2000. Lokalbeben-Tomographie der Umgebung von Antofagasta (Nordchile) sowie Betrachtung der Magnituden-Häufigkeits-Parameter in dieser Region, Diss. Fu-Berlin. Berliner Geowissentschaftliche Abhandlungen, 36, Reihe B.

Pilger, R. H., 1981. Plate reconstruction, aseismic ridges, and low-angle subduction beneath the Andes, Bull. Geol. Soc. Am. 92, 448-456.

Pilger, R.H., 1983. Kinematics of the South American subduction zone from global plate reconstructions, Geodynamics of the Eastern Pacific Region, Caribbean and Scotia Arcs, American Geophysical Union, Geodyn. Ser., 9, 113-126.

Ramos, V., 1999. Plate tectonic setting of the Andean Cordillera, Episodes, v.22, No.3, pp. 183-190.

Reutter, K.-J., Giese, P., Götze, H.-J., Scheuber, E., Schwab, K., Schwarz, G., Wigger, P., 1988. Structures and crustal development of the Central Andes between 21° and 25° S, The Southern Central Andes. Bahlburg, H., Breitkreuz, Ch., Giese, P., (eds.), Lecture Notes in Earth Sciences, 17: 231-261, Berlin.

Reutter, K-J., Scheuber, E., Chong G., 1996. The Precordilleran fault system of Chuquicamata, northern Chile: Evidence for reversals along arc parallel strike-slip faults, Tectonophysics, 259, 1-3 Spec. Iss, 213-228.

Sandoval, S., Kissling, E., Ansorge, J. and the SVEKALAPKO STWG, 2003. High-resolution body wave tomography beneath the SVEKALAPKO array: I. A-priori 3D crustal model and associated traveltime effects on teleseismic wavefronts. Geophys. J. Int. 153, 75–87.

Scheuber, E. and Reutter, K-J., 1992. Magmatic arc tectonics in the central Andes between 21° and 25°, Tectonophysics, 205, 127 – 140.

Scheuber, E., Bogdanic, T., Jensen, A., Reutter, K.-J., 1994. Tectonic development of the North Chilean Andes in relation to plate convergence and magmatism since the Jurassic, Tectonics of the Southern Central Andes: Reutter, K.-J., Scheuber, E., Wigger, P.J. (eds), Springer-Verlag, 121–139.

Scheuber, E. and Giese, P., 1999. Architecture of the Central Andes - a compilation of geoscientific data along a transect at 21°S, J. S. Am. Earth Sci. 12, pp. 103–107.

Scheuber, E., Mertmann, D., Ege, H., Silva, P., Heubeck C., Reutter K-J. & Jacobshagen, V., 2006. Exhumation and basin development related to formation of the central Andean plateau, 21°S, in: The Andes: Active Subduction Orogeny, Editors: O. Oncken, G. Chong, G. Franz, P. Giese, H.J. Götze, V.

Ramos, M. Strecker,, P. Wigger., pp 285-301. Springer-Verlag.

Schilling, F. R, Giese, P., Patzig, R., Brasse, H., Rietbrock, A. Wigger, P., Asch, G., Kind, R., Haberland, C., 2000. Fluid/Rock interactions in the Central Andean subduction zone imaged by geophysical observations, Latein Amerika Kollokium, Ext. Abstract, Stuttgart.

Schmitz, M., Lessel, K., Giese, P., Wigger, P., Araneda, M., Bribach, B., Graeber, F., Grunewald, S., Haberland, C., Lüth, S., Röwer, P., Ryberg, T., Schulze, A., 1993. The crustal structure beneath the Central Andean forearc and magmatic arc as derived from seismic studies – the PISCO 94 experiment in northern Chile (21°-23°S), J. S. Am. Earth Sci. 12, 237-260.

Schurr, B., Asch, G., Rietbrock, A., Kind, R., Pardo, M., Heit, B., Monfret, T., 1999. Seismicity and average velocities beneath the Argentine Puna plateau, Geophys. Res. Lett., 26, 3025-3028.

Schurr, B., 2000. Seismic structure of the central Andean subduction zone from local earthquake data, Ph.D Thesis, Freie Universitaet Berlin, Scientific Technical Report, 09/00, GeoForschungsZentrum, Potsdam.

Schurr, B., Asch, G., Rietbrock, A., Trumbull, R., Haberland, C., 2003. Complex patterns of fluid and melt transport in the central Andean subduction zone revealed by attenuation tomography, Earth Planet. Sci. Lett. 215, 105-119.

Schurr, B. and Rietbrock, A., 2004. Deep seismic structure of the Atacama Basin, northern Chile, Geophys. Res. Lett., 31, doi:10.1029/2004GL019796.

Schurr, B., Rietbrock , A., Asch, G. Kind, R., Oncken, O., 2006. Evidence for lithospheric detachment in the central Andes from local earthquake tomography, Tectonophysics, 415 (2006) 203–223.

Sempere, T., Herail, G., Oller, J., Bonhomme, M. G., 1990. Late Oligocene-early Miocene major tectonic crisis and related basins in Bolivia, Geology, 18, 946 – 949.

Sempere, T., Butler, R. F., Richards, D.R., Marshall, L.G., Sharp, W., Swisher, C., 1997. Stratigraphy and chronology of Upper Cretaceous-lower Paleogene strata in Bolivia and northwest Argentina, Geol. Soc. Am. Bull. 109, 709-727.

Stammler, K., 1993. SeismicHandler - programmable multichannel data handler for interactice and automatic processing of seismological analyses, Comp. Geosciences, 19, 135-140.

Troeng, B., Soria, E., Claure, H., Mobarec, R.,, Murillo, F., 1994. Descubrimiento de basamento precámbrico en la Cordillera Occidental Altiplano de los Andes Bolivianos, Mem. del XI Cong. Geol. Bol., 231-238.

Turcotte, D. L., Schubert, G., 1982. Geodynamics, Chapter 4: Applications of continuum physics to geological problems. John Wiley & Sons, New York.

Victor, P., Oncken, O., Glodny, J., 2004. Uplift of the western Altiplano plateau: Evidence from the Precordillera between 20° and 21°S (northern Chile), Tectonics, 23 doi:10.1029/2003TC001519.

Watts, A. B., Lamb, S.H., Fairhead, J. D., Dewey, J. F., Lithospheric flexure and bending of the central Andes, 1995. Earth Planet. Sci. Lett., 134, 9-21.

Whitman, D., Isacks, B., Kay, S.M., 1996. Lithospheric structure and along-strike segmentation of the Central Andean Plateau; seismic *Q*, magmatism, flexure, topography and tectonics, Tectonophysics, 259, 1-3: 29-40.

Wigger, P., Schmitz, M., Araneda, M., Asch, G., Baldzuhn, S., Giese, P., Heinsohn, W., Martinez, E., Ricaldi, E., Röwer, P., Viramonte, J., 1994. Variation of the crustal structure of the southern Central Andes deduced from seismic refraction investigations, Tectonics of the southern Central Andes, in K.-J. Reutter, E. Scheuber, P.J. Wigger (Eds), Springer-Verlag, New York, pp. 23-48.

Wittlinger, G., Tapponier, P., Poupinet, G., Mei, J., Danian, S., Herquel, G., Masson, F., 1998. Tomographic Evidence for Localized Lithospheric Shear along the Altyn Tagh Fault, Science 282, 74-76.

Woelbern, I., Heit, B., Yuan, X., Asch, G., Kind, R., 2007. Receiver function images from the Moho and the slab below the Altiplano and Puna plateaus in the Central Andes (submitted to Geophysical Journal International).

Yuan, X., S. V. Sobolev, R. Kind, O. Oncken and Andes Seismology Group, 2000. New constraints on subduction and collision processes in the Central Andes from comprehensive observations of P to S converted seismic phases, Nature, 408, 958-961.

Yuan, X., Sobolev, S.V, Kind, R., 2002. Moho topography in the central Andes and its geodynamic implications, Earth Planet. Sci. Lett., 199, 389-402.

Zandt, G., Beck, S.L., Ruppert, S.R., Ammons, C.J., Rock, D., Minaya, E., Wallace, T.C., Silver, P.G., 1996. Anomalous crust of the Bolivian Altiplano, Central Andes: Constraints from broadband regional seismic waveforms, Geophys. Res. Lett., 23, 1159-1162.

Zandt, G., Leidig, M., Chmielowski, J., Beaumont, D., Yuan, X., 2003. Seismic detection and Characterization of the Altiplano-Puna Volcanic Complex, Central Andes, PAGEOPH 160, 789-807.

Figure captions

Figure 1: Configuration of the observation system. (A): Map view of the station distribution along 21°S. Stations are indicated with different colour triangles according to the values of average residuals after corrections for topography and Moho discontinuity. Positive residuals (red triangles) correspond to areas of slow seismic velocities. Negative values are high velocities (blue triangles). Ray paths down to the depth of 300 km are shown by grey lines. Morphological units (dashed lines) along the profile are: C.C: Coastal Cordillera; L.V.: Longitudinal Valley; P.C.: Precordillera; W.C.: Western Cordillera; Altiplano; E.C.: Eastern Cordillera; I.A.: Interandean; S.A.: Subandean; C.P.: Chaco Plain. (B): Projection of the ray paths onto the vertical profile with an exaggerated topography scale from station coordinates. The bold black line in the vertical section shows the Moho depth (Yuan et al., 2000 and 2002) used in this study to correct the residuals.

Figure 2: Distribution of teleseismic events (red dots) recorded by the network between 2002 and 2004. Note the inhomogeneous distribution north and south and the similar distribution east and west of our study area (green square).

Figure 3: Screen showing the vertical component of *P*- waveforms for one event aligned by picked times after restitution and filtering, using Seismic Handler Motif (SHM, Stammler, 1993).

Figure 4: Examples of grid construction for P- waves according to ray density at three depth levels (i.e. 30, 65 and 125 km). Colours show normalized values of the ray density. 1 in the scale corresponds to 128 km of summary ray path in a cube of dimensions 20x20x20 km.

Figure 5: Checkerboard test for investigation of the horizontal resolution. The initial model is presented on the top plot on the left. The other maps show the results of reconstruction in various depth levels.

Black triangles represent the distribution of stations. Dotted lines show the position of the initial anomalies. Thin lines are political borders. The upper left plot shows the position of the profile over a distance of 700 km used to present the results from Figures 6 to 9.

Figure 6: Checkerboard test for investigation of the vertical resolution along the profile shown in Figure 5. A): Initial synthetic model. B): Results of reconstruction.

Figure 7: A) Initial model for synthetic tests to check the capacity to resolve realistic patterns expected in our study region. Different coloured bodies represent low- and high- velocity anomalies in the lithosphere (continental crust and upper mantle) and the position of the slab. B): Reconstruction results along the profile shown in Figure 5.

Figure 8: Synthetic test showing the poor capacity of the teleseismic approach to reconstruct the real shape of the slab. A) Initial position of the slab including earthquake hypocenters are taken from Engdahl et al. (1998). B) Results of the reconstruction along the profile shown in Figure 5 using data without noise, which provides 97% of variance reduction..

Figure 9: Results of the inversion for *P*- wave residuals with and without a-priori information, presented as vertical sections. A) Inversion of the observed data for a 1D model. B) Superposition of the inversion results for "no-slab" residuals with the addition of the slab inversion results. C) The final section showing the combination of the inversion results for "no-slab" residuals with the model for the slab. Position of the profile is shown in Figure 5.

Figure 10: Horizontal sections of the resulting *P*-velocity anomalies in three depth levels (40 km, 80 km and 160 km depth). These results correspond to the case where a-priori information of the slab is used. Position of recent volcanoes is shown by red triangles. Stations are shown by black triangles.

Figure 11 A) *P*- velocity anomalies. Dashed lines: receiver function Moho and slab (Yuan et al, 2000; Heit, 2005; Woelbern et al., 2007). Small triangles are the stations along the profile. B) Schematic cartoon showing the interpreted anomalies. The upper 20km without resolution, the high velocity fore-arc block; QBBS: Quebrada Blanca Bright Spot; High velocity Neogene volcanics-Precambrian basement; ALVZ: Altiplano Low Velocity Zone; Brazilian Shield on the eastern side of the profile. Low velocity materials are located beneath the Moho (dashed line) and beneath the LAB -Lithosphere-Asthenosphere Boundary- (green line) after Heit et al. (2007). Major lineaments and fault systems are thought to be responsible for velocity variations in the crust. UKFZ: Uyuni-Kenayani Fault Zone; MAT: Main Andean Trust. Abbreviations from geological provinces are the same as in Figure 1.

FIGURES 1 -11

A)

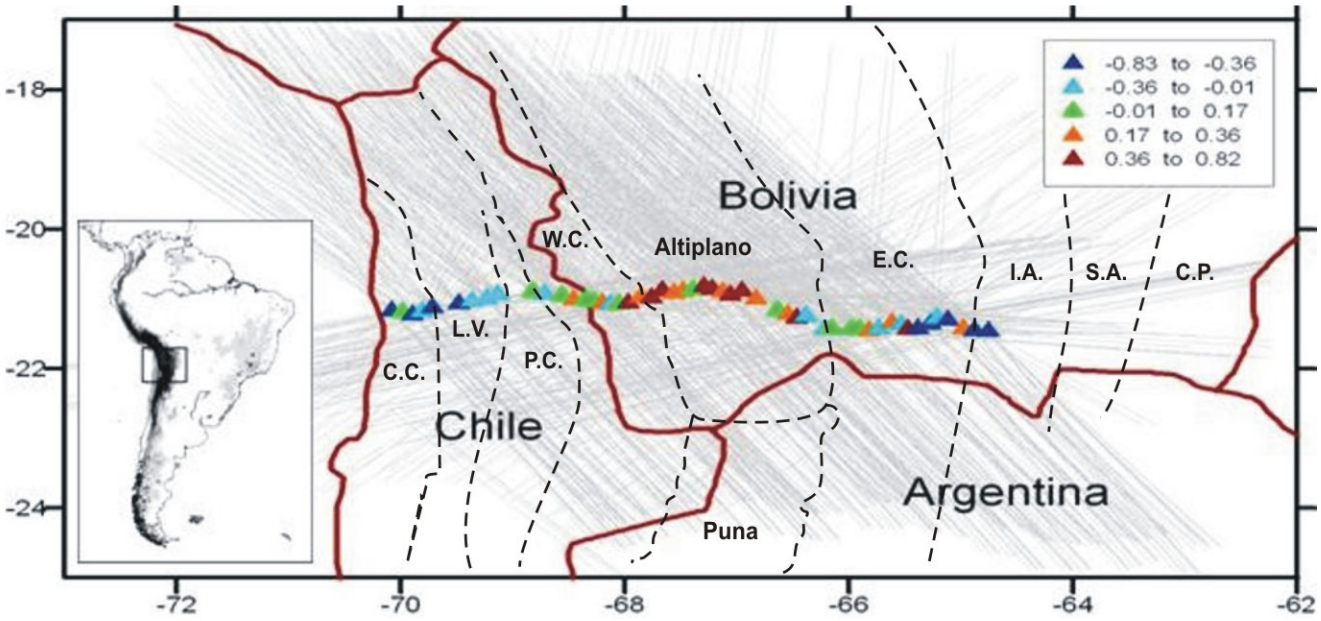

B)

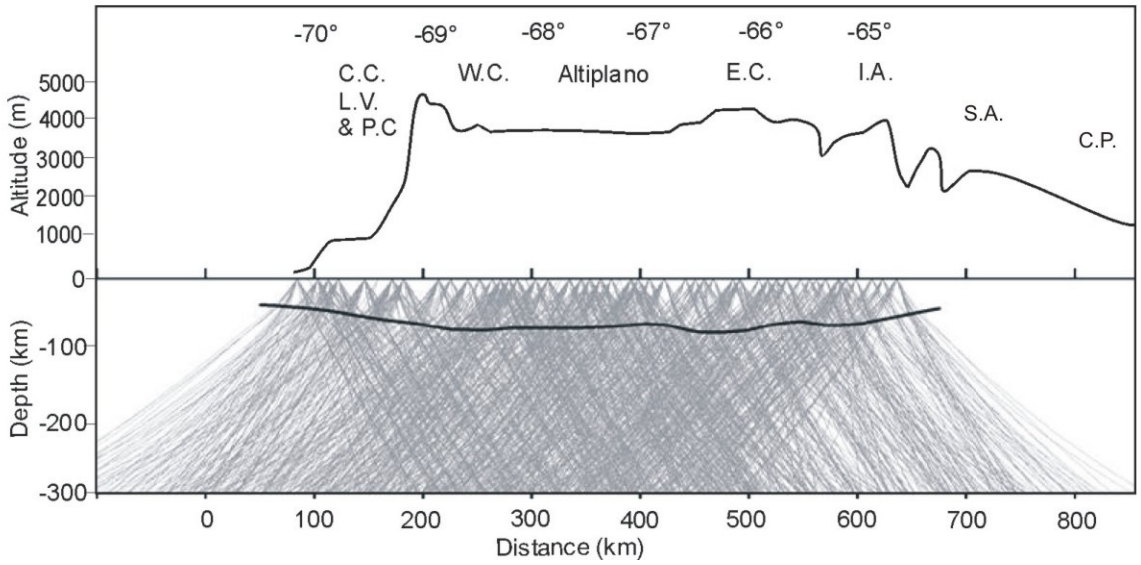

Figure 1

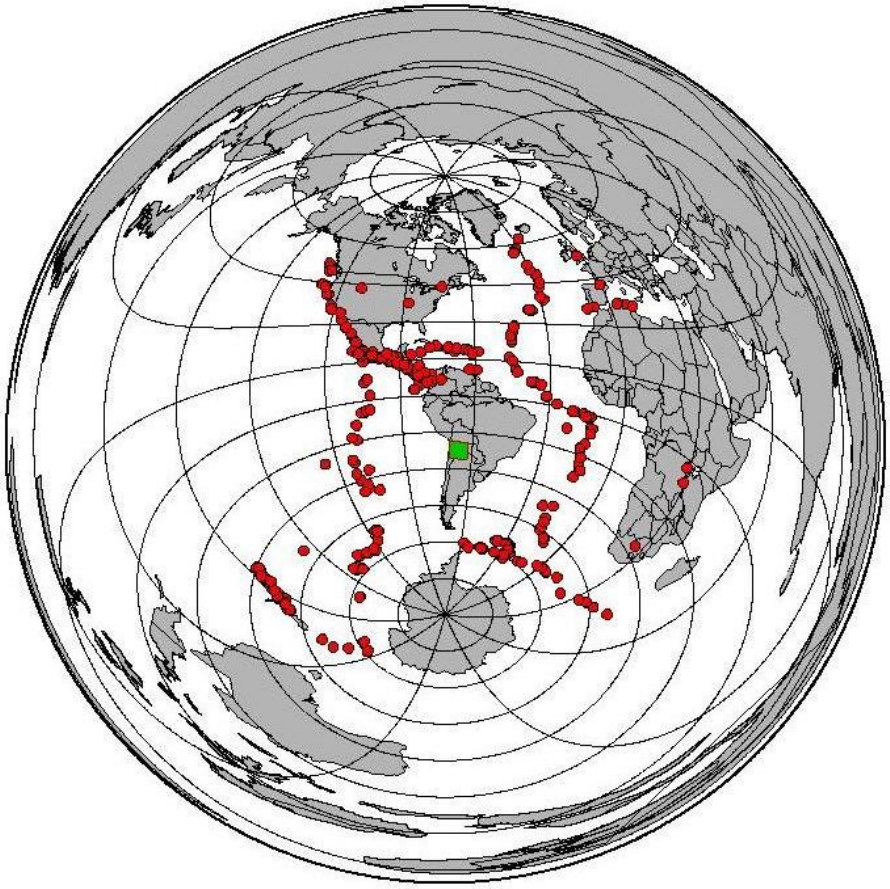

Figure 2

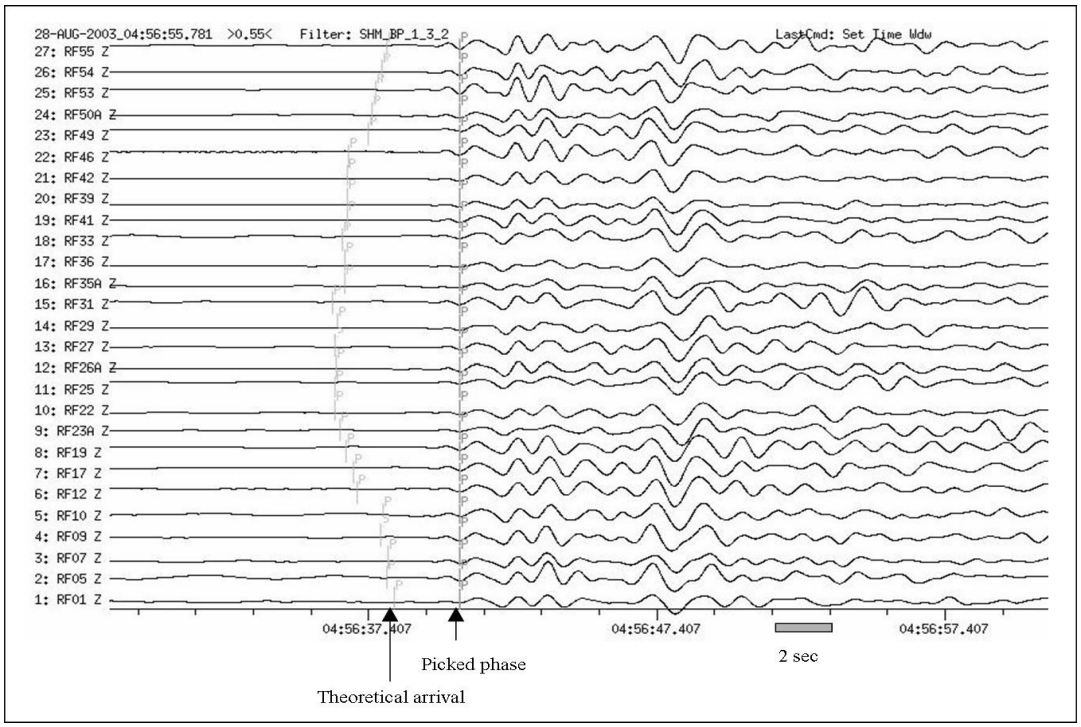
28-AUG-2003_04:56:55.781 >0.55< Filter: SHM_BP_1_3_2
LastCmd: Set Time Wdw
27: RF55 Z
26: RF54 Z
25: RF53 Z
24: RF50A Z
23: RF49 Z
22: RF46 Z
21: RF42 Z
20: RF39 Z
19: RF41 Z
18: RF33 Z
17: RF36 Z
16: RF35A Z
15: RF31 Z
14: RF29 Z
13: RF27 Z
12: RF26A Z
11: RF25 Z
10: RF22 Z
9: RF23A Z
8: RF19 Z
7: RF17 Z
6: RF12 Z
5: RF10 Z
4: RF09 Z
3: RF07 Z
2: RF05 Z
1: RF01 Z
04:56:37.407
04:56:47.407
04:56:57.407
2 sec
Picked phase
Theoretical arrival

Figure 3

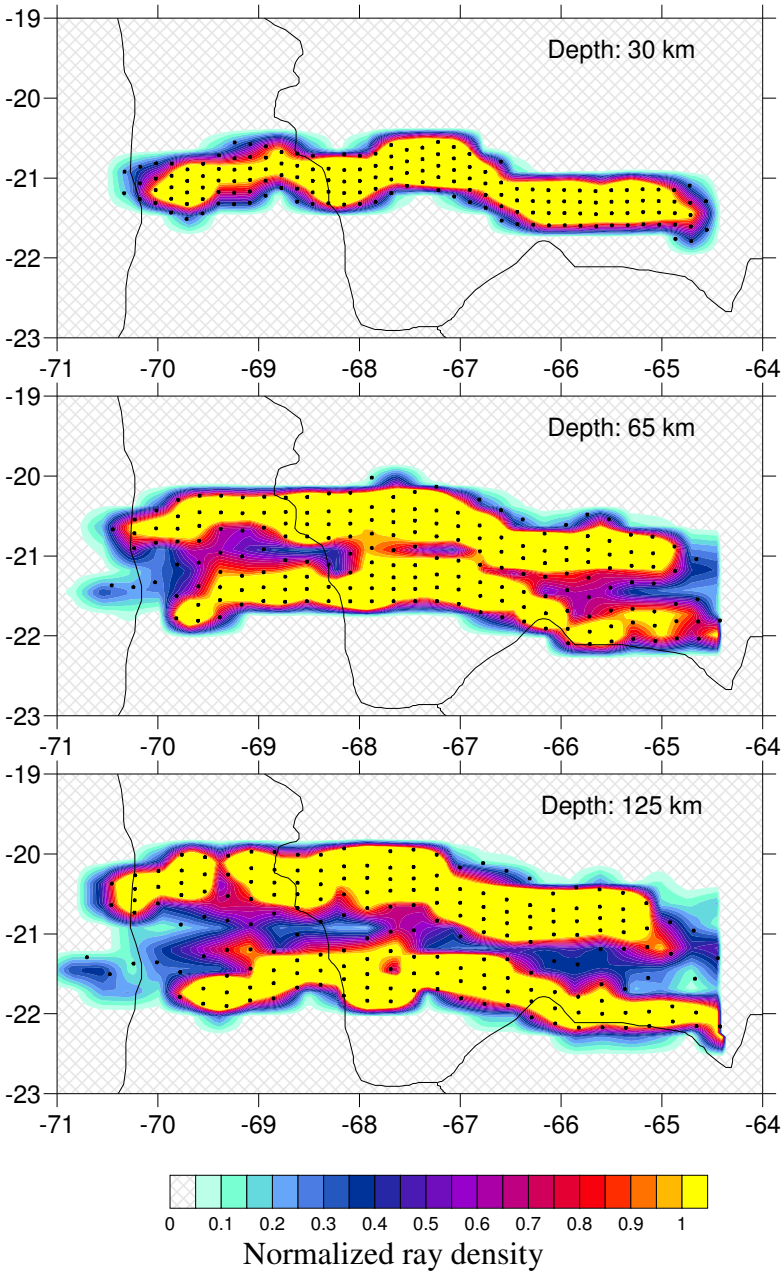
Depth: 30 km
Depth: 65 km
Depth: 125 km
-19
-20
-21
-22
-23
-71
-70
-69
-68
-67
-66
-65
-64
0
0.1
0.2
0.3
0.4
0.5
0.6
0.7
0.8
0.9
1
Normalized ray density

Figure 4

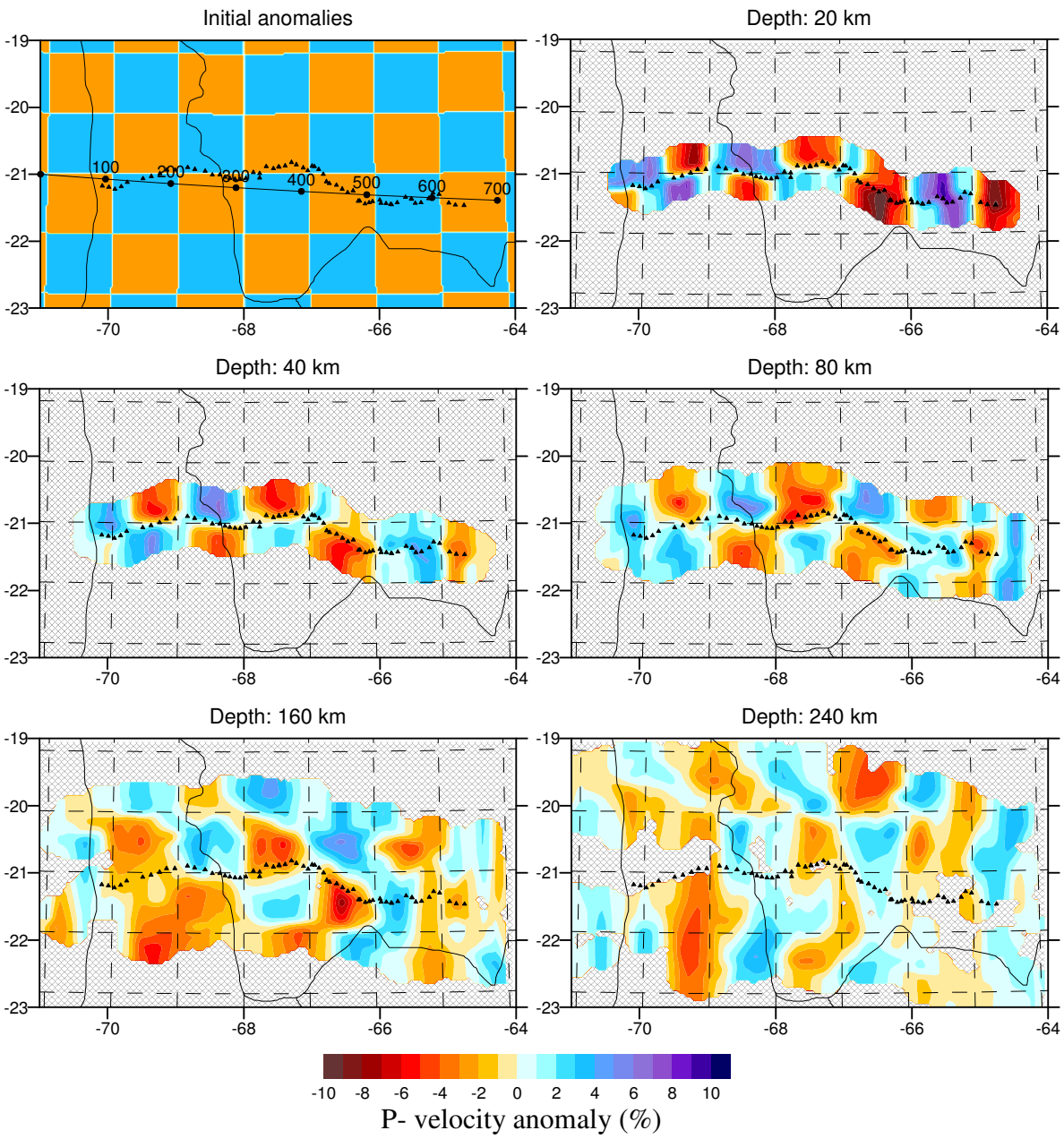
Initial anomalies
Depth: 20 km
Depth: 40 km
Depth: 80 km
Depth: 160 km
Depth: 240 km
100
200
300
400
500
600
700
-19
-20
-21
-22
-23
-70
-68
-66
-64
-10 -8 -6 -4 -2 0 2 4 6 8 10
P- velocity anomaly (%)

Figure 5

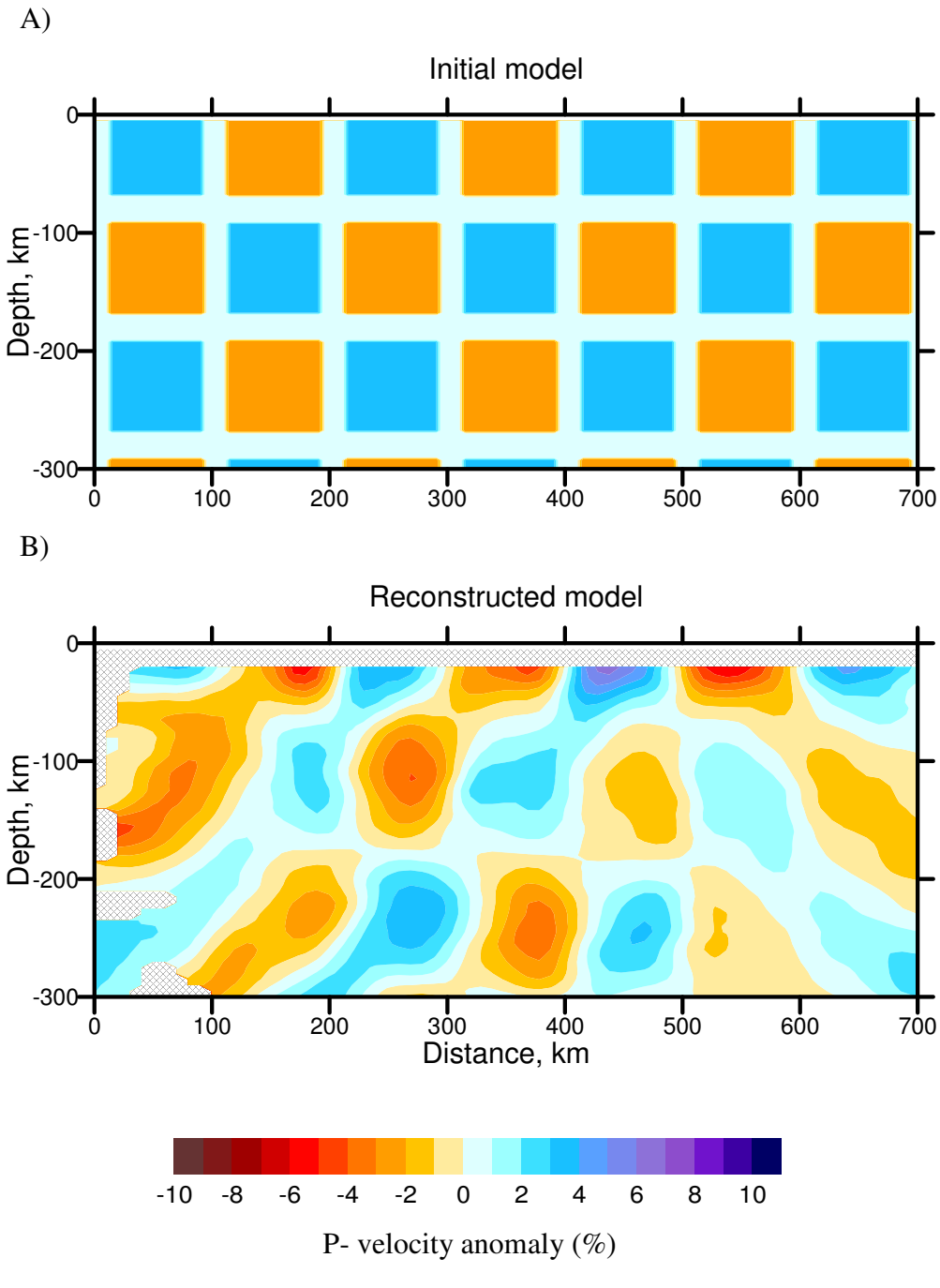
A)
Initial model
Depth, km
0
-100
-200
-300
0
100
200
300
400
500
600
700
B)
Reconstructed model
Depth, km
0
-100
-200
-300
0
100
200
300
400
500
600
700
Distance, km
-10
-8
-6
-4
-2
0
2
4
6
8
10
P- velocity anomaly (%)

Figure 6

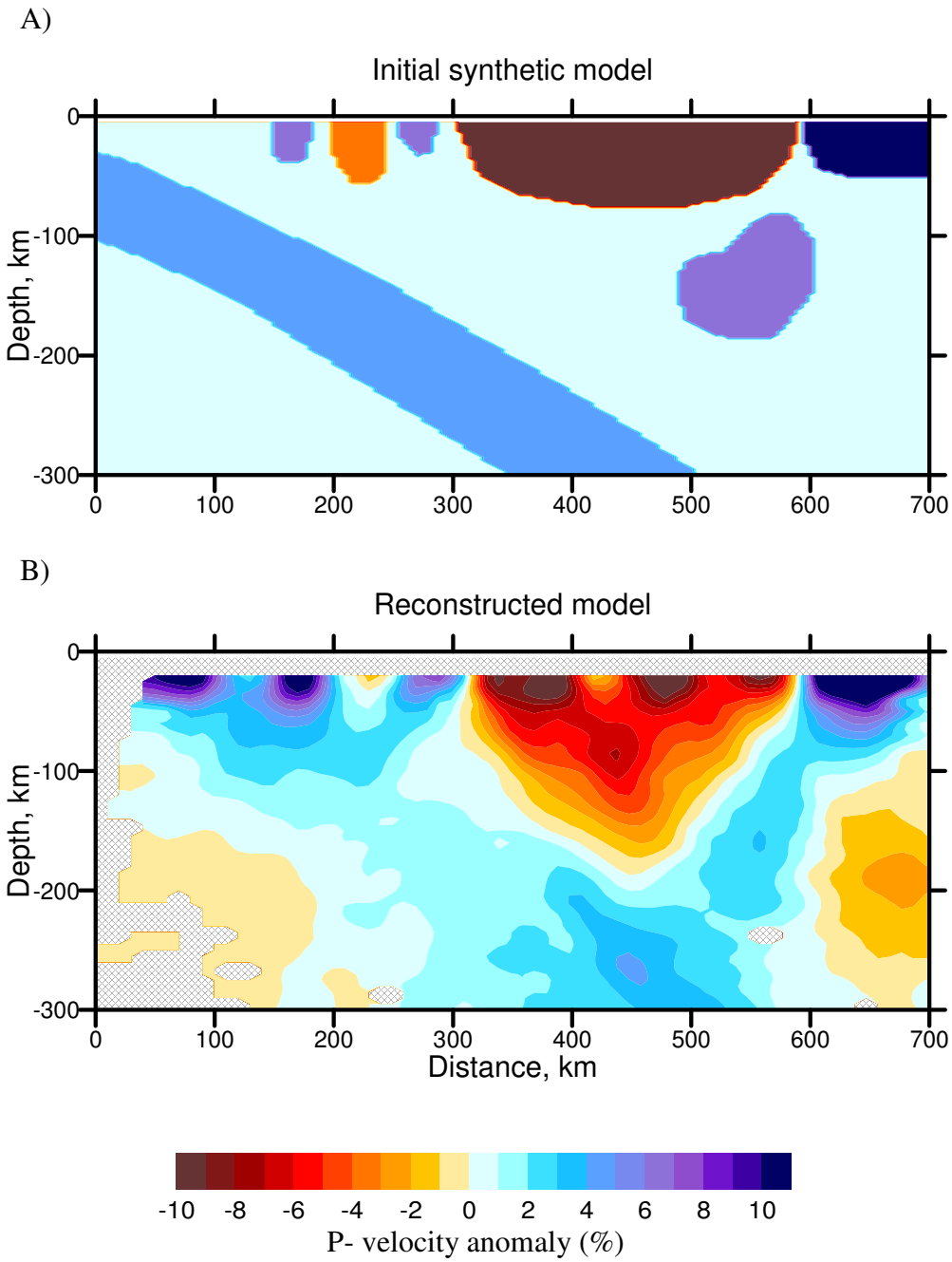
A)
Initial synthetic model
Depth, km
0
-100
-200
-300
0
100
200
300
400
500
600
700
B)
Reconstructed model
Depth, km
0
-100
-200
-300
0
100
200
300
400
500
600
700
Distance, km
-10
-8
-6
-4
-2
0
2
4
6
8
10
P- velocity anomaly (%)

Figure 7

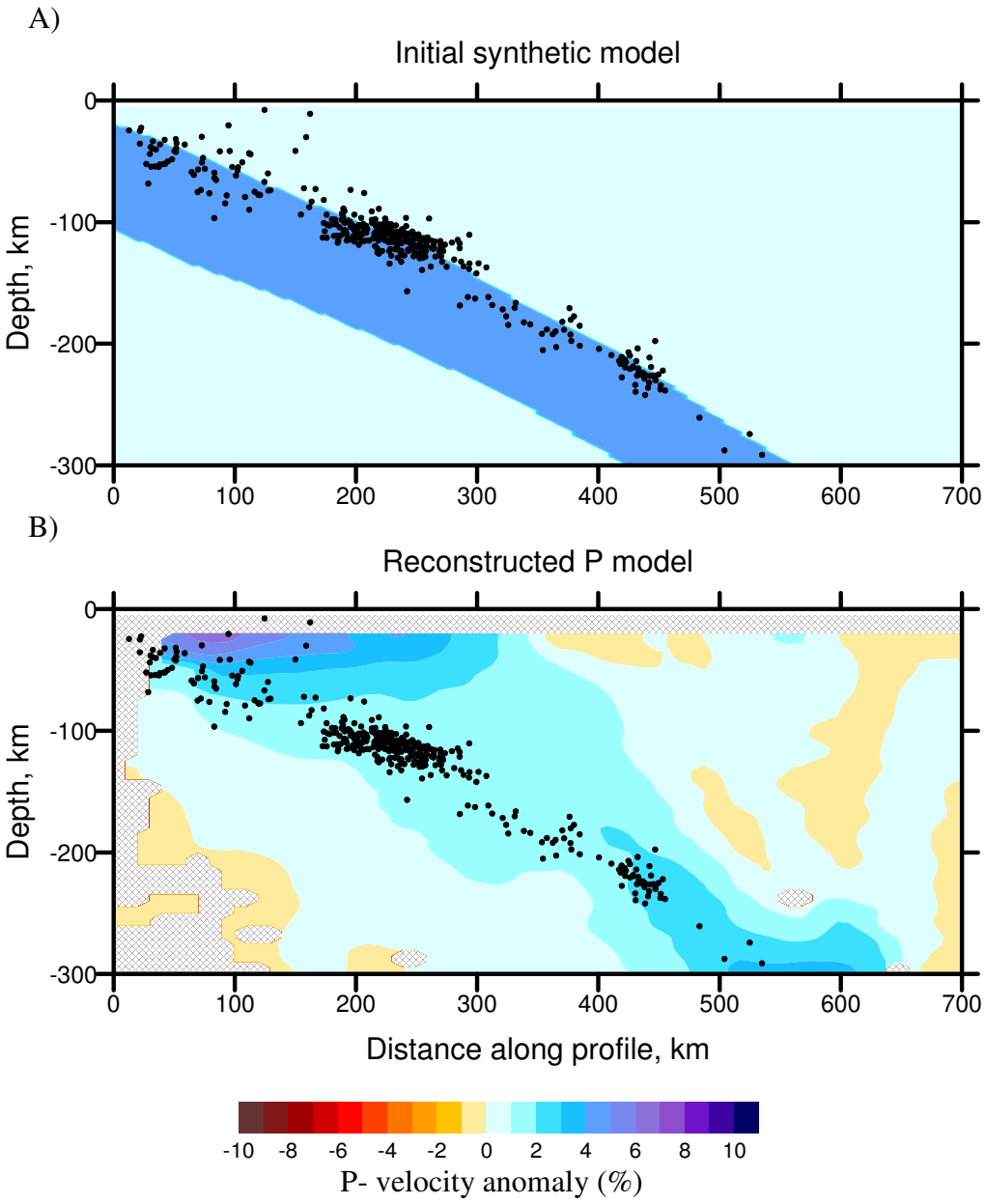
A)
Initial synthetic model
Depth, km
0
-100
-200
-300
0
100
200
300
400
500
600
700
B)
Reconstructed P model
Depth, km
Distance along profile, km
-10
-8
-6
-4
-2
0
2
4
6
8
10
P- velocity anomaly (%)

Figure 8

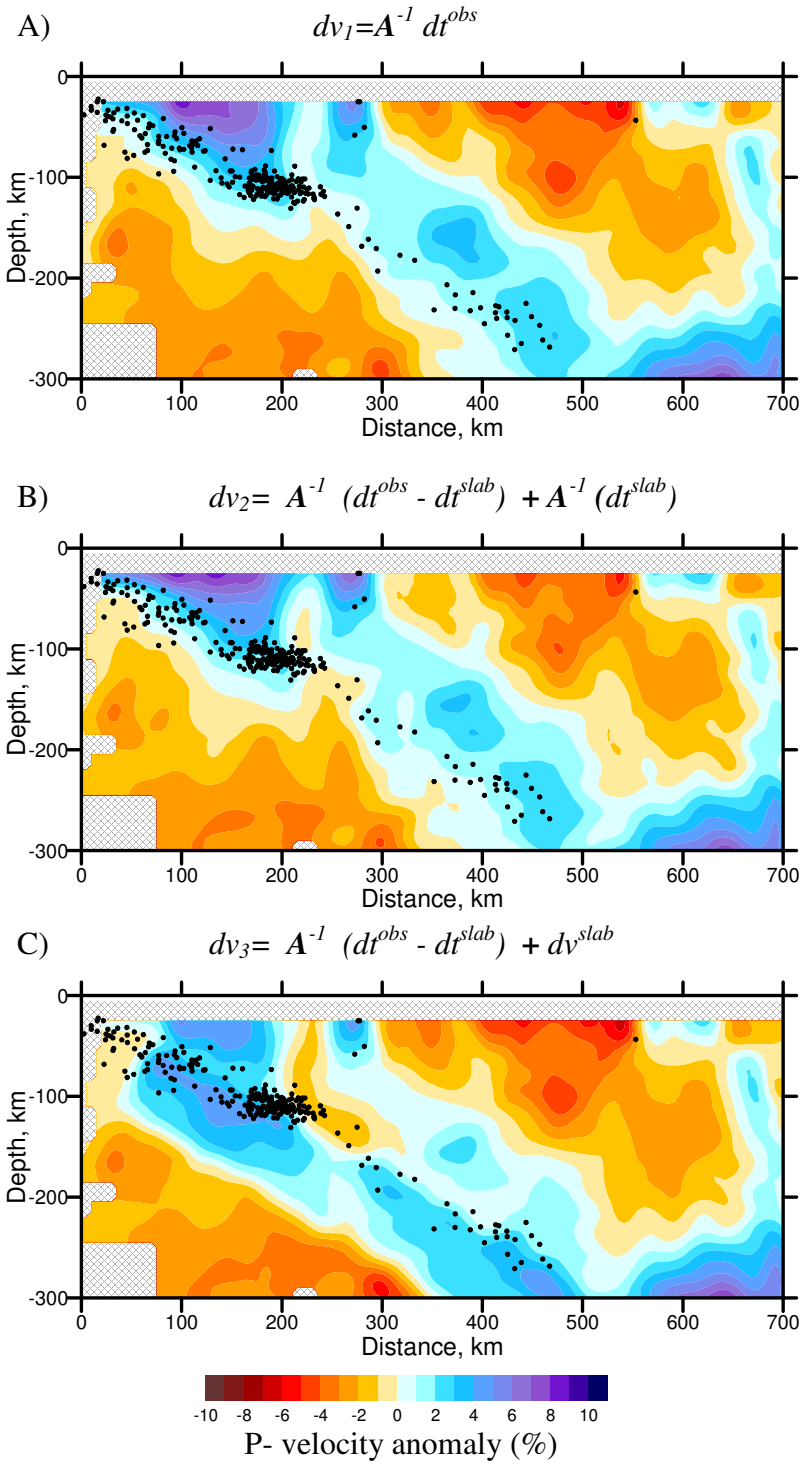
A)
$dv_1=A^{-1}\ dt^{obs}$
B)
$dv_2= A^{-1}\ (dt^{obs} - dt^{slab}) + A^{-1}\ (dt^{slab})$
C)
$dv_3= A^{-1}\ (dt^{obs} - dt^{slab}) + dv^{slab}$
Depth, km
0
-100
-200
-300
0
100
200
300
400
500
600
700
Distance, km
-10 -8 -6 -4 -2 0 2 4 6 8 10
P- velocity anomaly (%)

Figure 9

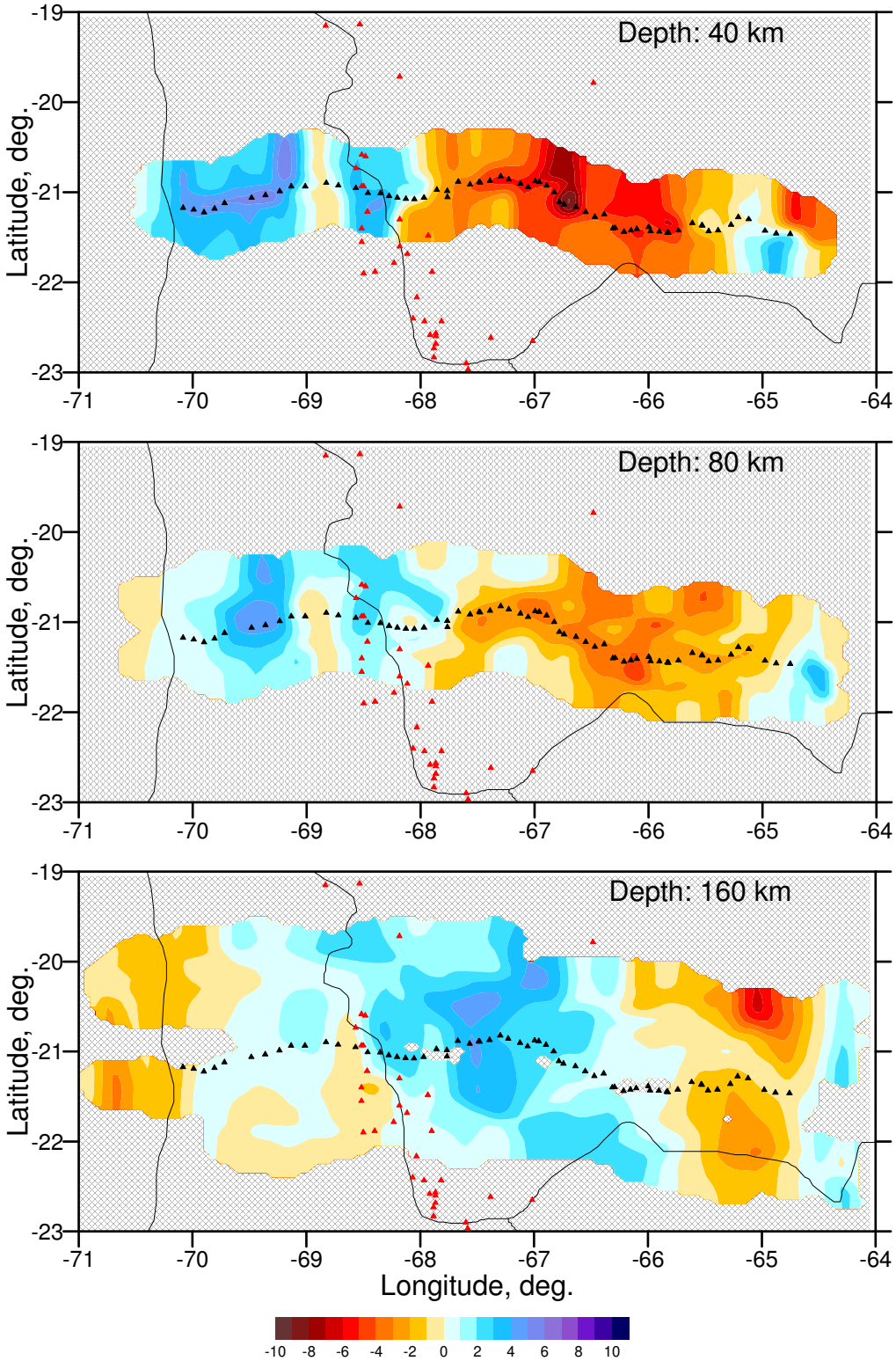
Depth: 40 km
Depth: 80 km
Depth: 160 km
Latitude, deg.
Longitude, deg.
-19
-20
-21
-22
-23
-71
-70
-69
-68
-67
-66
-65
-64
-10 -8 -6 -4 -2 0 2 4 6 8 10
P- velocity anomaly (%)

Figure 10

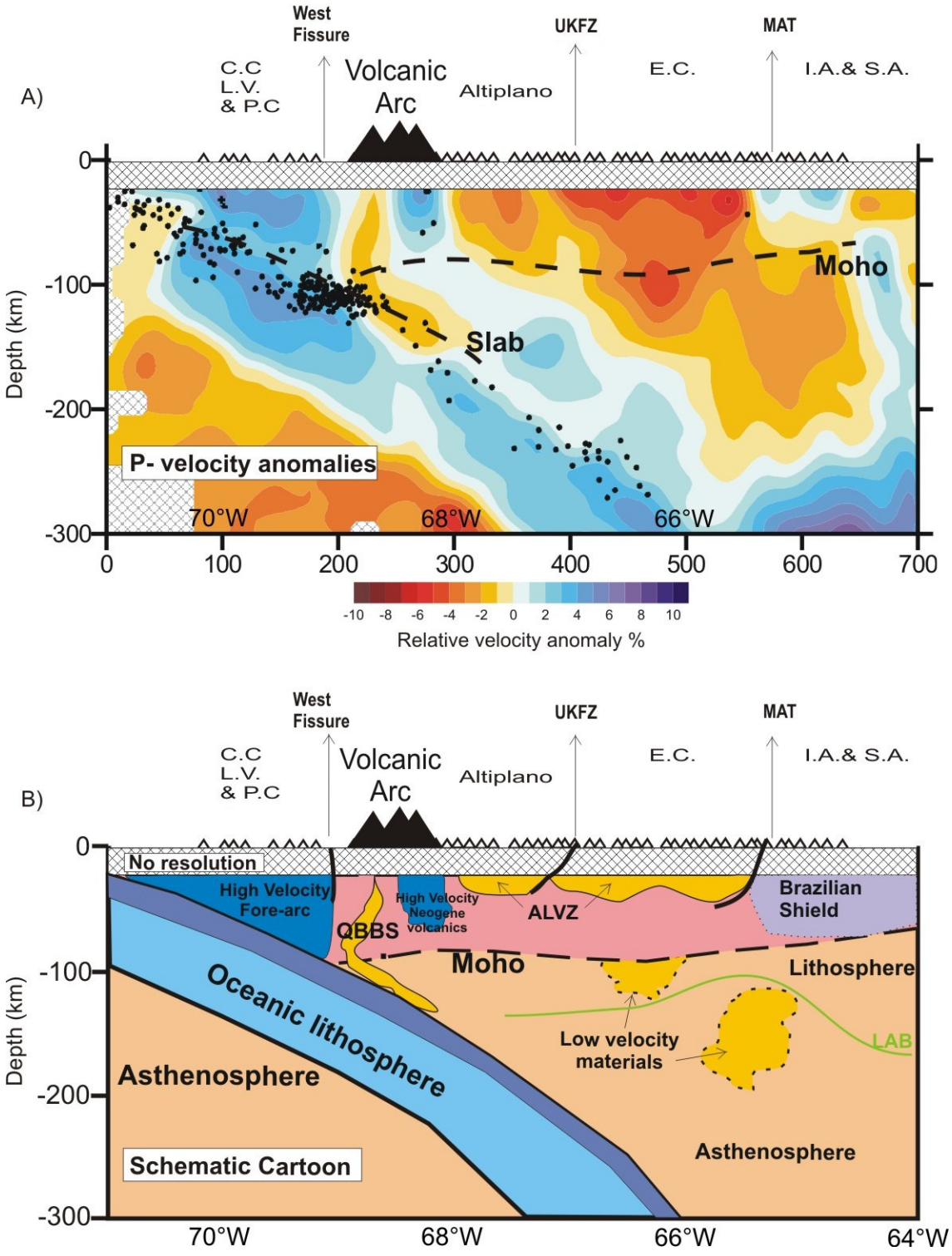
A)
West Fissure
UKFZ
MAT
C.C L.V. & P.C
Volcanic Arc
Altiplano
E.C.
I.A.& S.A.
Moho
Slab
P- velocity anomalies
Depth (km)
0
-100
-200
-300
70°W
68°W
66°W
0
100
200
300
400
500
600
700
-10 -8 -6 -4 -2 0 2 4 6 8 10
Relative velocity anomaly %
B)
West Fissure
UKFZ
MAT
C.C L.V. & P.C
Volcanic Arc
Altiplano
E.C.
I.A.& S.A.
No resolution
High Velocity Fore-arc
High Velocity Neogene volcanics
QBBS
ALVZ
Brazilian Shield
Moho
Lithosphere
Oceanic lithosphere
Low velocity materials
LAB
Asthenosphere
Asthenosphere
Schematic Cartoon
Depth (km)
0
-100
-200
-300
70°W
68°W
66°W
64°W

Figure 11